UAV-based LiDAR Bathymetry at an Alpine Mountain Lake

Katja Richter*, David Mader, Hannes Sardemann, Hans-Gerd Maas

Institute of Photogrammetry and Remote Sensing, Dresden University of Technology Helmholtzstraße 10, 01069 Dresden, Germany

Keywords: UAV-based LiDAR bathymetry, full-waveform stacking, 3D water turbidity fields.

Abstract

LiDAR bathymetry provides an efficient and comprehensive way to capture the topography of water bodies in shallow water areas. However, the penetration depth of this measurement method into the water column is limited by the medium water and water turbidity, resulting in a limited detectability of the bottom topography in deeper waters. An increase of the analyzable water depth is possible by the use of extended evaluation methods, in detail full-waveform stacking methods. So far, however, this has only been investigated for water depths of up to 3.50 m due to water turbidity. In this article, the potential of these extended data processing methods is investigated on an alpine mountain lake with low water turbidity and thus high analyzable water depth. Compared to the standard data processing, the penetration depth could be significantly increased by $58\,\%$. In addition, methods for depth-resolved water turbidity parameter determination on the basis of LiDAR bathymetry data were successfully tested.

1. Introduction

LiDAR bathymetry is a method for the efficient and area-wide acquisition of water bottom topography in shallow coastal areas and inland waters. The recent development of compact, lightweight, and sufficiently powerful bathymetric laser scanners enables their use on UAVs (uncrewed aerial vehicles). In this way, the water bottom topography can be mapped flexibly, cost-efficiently and with high resolution. Investigations on the application potential of UAV-based LiDAR bathymetry show that study areas can be scanned time-efficiently, with high point density and high accuracy (Mandlburger et al., 2020, 2022).

The penetration depth of LiDAR bathymetry is limited by the attenuation of the green laser pulse in the water medium and the water turbidity. Recently, novel processing methods for full-waveform LiDAR bathymetry data have been developed to extend the depth range and to derive additional information from the measurement data. Compared to standard processing methods, higher penetration depths and better coverage of the water bottom with measurement points can be achieved (Mader et al., 2021, 2023a,b). In addition, information on water turbidity can be derived (Richter et al., 2017, 2021, 2022). However, existing studies investigating the potential of these methods are limited to airborne LiDAR bathymetry (ALB) data in shallow water areas with high water turbidity, e.g. from the federal waterway Elbe in Germany and the German Wadden Sea National Park. The maximum analyzable water depth in these data sets was approximately $3.50\,\mathrm{m}$ due to the high water turbidity.

In this study, the novel processing methods are applied to a data set with a large analyzable water depth larger than $10\,\mathrm{m}$. For this purpose, a UAV-based LiDAR measurement campaign was carried out on an alpine mountain lake characterized by low water turbidity and large water depth. The UAV-based LiDAR bathymetry data differs from the conventional ALB data in terms of point density and footprint size. The study therefore also examines the application of the new processing methods to a data set with a higher point density and smaller footprint.

The paper is structured as follows. The study area and the measurement campaign are presented in Section 2. Section 3 describes the novel full-waveform processing methods for the derivation of water bottom topography. The determination of 3D turbidity parameter fields is presented in Section 4. The paper ends with a conclusion in Section 5.

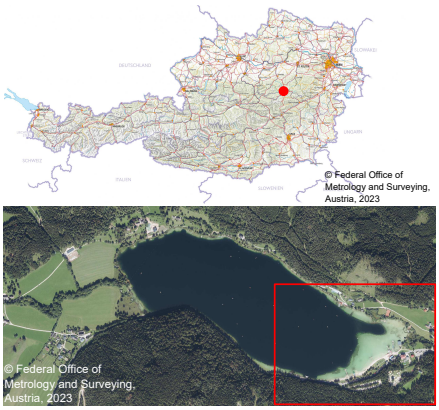

Figure 1. Top: Location of Lake Erlauf in Austria. Bottom: Location of the study area in the eastern part of Lake Erlauf.

2. Study area and data acquisition

The study area is a part of the Lake Erlauf, an alpine mountain lake near the town Mariazell in Austria (Fig. 1). The UAV-based LiDAR bathymetry data was acquired in summer 2022 using a RIEGL VQ-840-G on an UAV. The study area covers approximately $350\,\mathrm{m} \times 350\,\mathrm{m}$ and was flown with six overlapping flight strips with a swath width of approximately $100\,\mathrm{m}$. The flight altitude was approximately $135\,\mathrm{m}$ above the water surface. The mean point density was approximately 160 points per m^2, whereby the point distribution is inhomogeneous due to the elliptical scan pattern and the overlapping flight strips. The measurement campaign comprised two flights over the same measurement area with different beam divergence angles ($1\,\mathrm{mrad}$ and $4\,\mathrm{mrad}$ corresponding to a footprint size of $13.5\,\mathrm{cm}$ and $54\,\mathrm{cm}$ at the water surface). The sampling time interval was $0.503\,\mathrm{ns}$, which corresponds to a 3D distance of $5.64\,\mathrm{cm}$ under water.

* Corresponding author

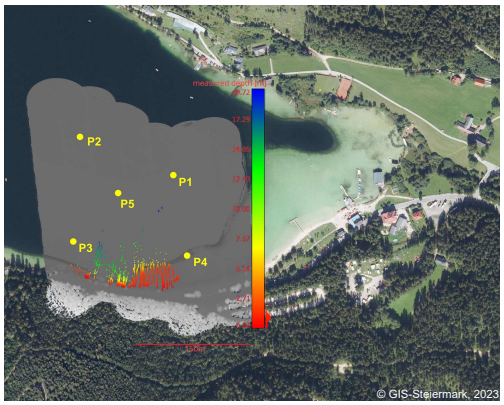

Figure 2. Measurement data to validate the results of full-waveform stacking and depth-resolved water turbidity parameter estimation.

For validation purposes, hydroacoustic measurements were carried out in the study area. A vertical echo sounder (EchoLogger ECT400) installed on an uncrewed water vehicle (UWV) was used to measure the water bottom topography profile by profile (Sardemann et al., 2018). The measurement frequency was 1 Hz, resulting in point distances of 0.5 m up to 1.2 m along a profile, depending on the speed of the UWV. The distances between the profiles were generally less than 8 m. The depths measured with the echo sounder were corrected using water temperatures measured with a CTD probe. The corrected echo sounder measurements were then georeferenced with the IMU and RTK positions of the UWV. However, the temperature measurements were only made at three locations in the deep part of the lake. Deviating temperatures in the shallow water may affect the accuracy of the depth measurements. It is also affected by the unknown characteristics and variable geometry of the water bottom (Anderson et al., 2007). As the hydroacoustic measurements generally have no superior accuracy with respect to ALB, they cannot be used as reference measurements. However, they are well suited for plausibility checks of the UAV-based LiDAR bathymetry measurements.

In addition, various water property parameters were determined at five measuring points using in-situ measuring methods. Photosynthetically active radiation (PAR) was measured using a spherical quantum sensor. The chlorophyll concentration was determined using a fluorescence probe. Temperature, dissolved oxygen, pH-value, conductivity and water turbidity were measured with a CTD probe. The water transparency was determined using a Secchi disk (Secchi, 1864).

Fig. 2 provides an overview of the location of the measurements. The vertical echo sounder measurements on the south shore are color coded according to their water depth. The yellow dots P1 – P5 show the locations of the in-situ water property measurements.

3. Derivation of water bottom topography using full-waveform stacking approaches

This section briefly introduces various methods of full-waveform processing. On the one hand, a brief overview of existing established methods for the extraction of object echoes in full-waveform signals is given (Section 3.1 and 3.2) and, on the other hand, the main features of the novel full-waveform processing approaches for detecting weak water bottom echoes are

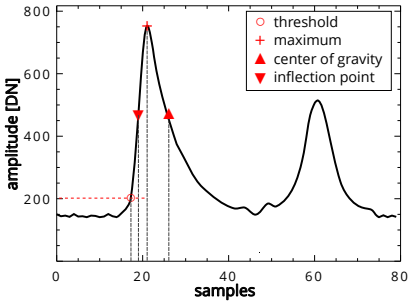

Figure 3. Full-waveform with conventional peak detectors. Figure according to Mader et al. (2021).

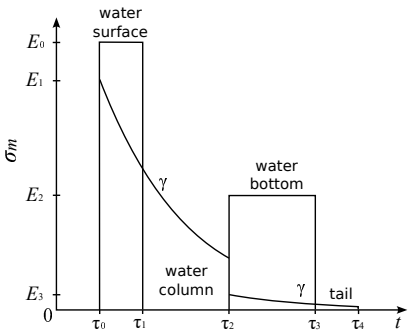

Figure 4. Principle of exponential decomposition; σ_m = model of the differential backscatter cross-section (dBCS); τ_i = time interval limits of the dBCS segments; E_i = amplitude values of the σ_m; γ = attenuation coefficient. Figure according to Schwarz et al. (2019).

presented (Section 3.3). The main difference between the standard methods and the novel full-waveform processing methods is that the isolated evaluation of the full-waveform data is replaced by a combined evaluation of neighboring full-waveforms to provide additional information about the water depth. The novel methods were used to analyze the UAV-based LiDAR bathymetry data set with a beam divergence angle of 1 mrad. For validation purposes, the results are compared with the hydroacoustically determined water depths (Section 3.4).

3.1 Conventional peak detection and decomposition

There are several methods to extract object echoes from full-waveform data. Wagner et al. (2004) and Wang et al. (2015) present basic methods for detecting object echoes in full-waveforms, including the threshold operator, the peak maximum, the center of gravity, and the inflection point (Figure 3).

A more complex method for estimating the peak position, peak amplitude and peak width is Gaussian decomposition (Wagner et al., 2006; Reitberger et al., 2009; Mallet and Bretar, 2009). However, this method is less suitable for analyzing LiDAR bathymetry data due to the specific signal characteristics caused by the influence of the water column on the signal. Schwarz et al. (2017, 2019) present the surface-volume-bottom method based on the exponential decomposition, which can extract water surface, water column, and water bottom echoes from the full-waveform signal (Figure 4).

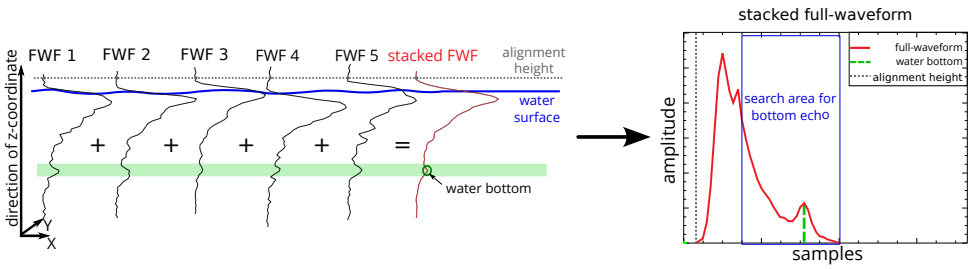

Figure 5. Principle of pseudo-waveform generation for sigFWFS. Pseudo-waveform for sigFWFS = stacked full-waveform. (Mader et al., 2021, 2023b).

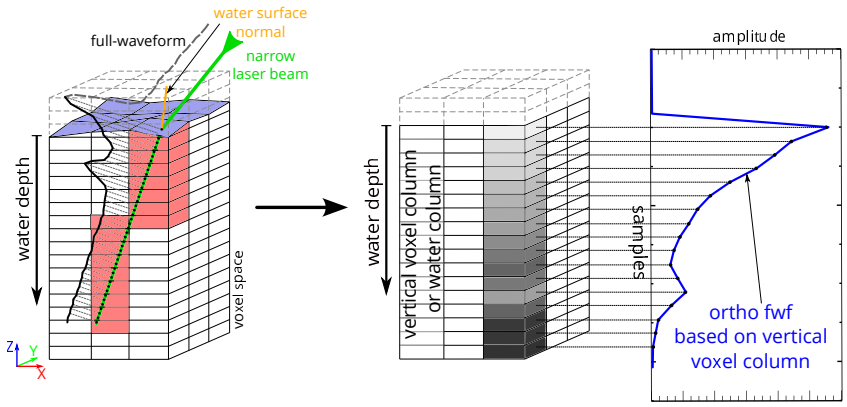

Figure 6. Principle of pseudo-waveform generation for volFWFS. Pseudo-waveform for volFWFS = ortho full-waveform. (Mader et al., 2023a,b).

3.2 Standard processing with commercial software packages

The terms standard processing and online waveform processing (OWP) are used here to refer to the real-time evaluation and post-processing by manufacturer software and other commercial software packages. The exact processing sequence in these software packages is only partially published (Pfennigbauer et al., 2009; Pfennigbauer and Ullrich, 2010). It can be assumed that both peak detectors and decomposition methods are used, also in combination.

3.3 Full-waveform stacking for the detection of weak water bottom echoes

Full-waveform stacking methods are based on the combined analysis of closely adjacent full-waveform data, which are accumulated into pseudo-waveforms. The pseudo-waveforms have an improved signal to noise ratio and therefore allow for more reliable detection of weak water bottom echoes. The non-linear signal-based and volumetric full-waveform stacking approaches (sigFWFS and volFWFS) presented in Mader et al. (2021) and Mader et al. (2023a) differ in the generation of the pseudo-waveform. The sigFWFS combines the complete signal characteristics of individual full-waveforms which are closely adjacent at the water surface (Fig. 5). The geometric direction of the laser pulses in the water column is not considered herin. In contrast, the volFWFS takes into account the geometric propagation of the laser pulses throughout the water column using a voxel space representation (Fig. 6). For the present study, a voxel size of $2\,\mathrm{m} \times 2\,\mathrm{m} \times 0.1\,\mathrm{m}$ was chosen. In both methods, the water bottom echoes in the individual full-waveforms are detected and extracted based on the water depth information of the pseudo-waveforms. Details on how the full-waveform stacking process works can be found in the literature cited above.

3.4 Results of water bottom topography derivation using sigFWFS and volFWFS

First, the results of sigFWFS and volFWFS are visually analyzed. Fig. 7 (a) and (b) show a top view of the extracted water bottom points. As can be clearly seen, the shallow water area (water depth $< 1.6\,\mathrm{m}$) was not extracted correctly. In the area marked in purple, the full-waveforms could not be correctly evaluated by the full-waveform stacking method due to their unusual shape. Figure 8 shows a characteristic full-waveform from the shallow water area in the study area, which differs significantly from a typical textbook form. Full-waveforms with very similar characteristics are also presented in Saylam et al. (2018) and explained with shallow water depths and very low water turbidity. Since the standard processing worked very well in the shallow water areas, the OWP data can be used there without any problems instead of the full-waveform stacking results.

Beyond the shallow water area, the bottom is characterized by a steep gradient. This is followed by a highly rugged zone that is not plausible (Fig. 7 (a) and (b), areas outlined in red). The filter methods optimized for moderately sloping water bottom topographies obviously failed here. In future work, the filtering methods will have to be adapted for steeply sloping water bottoms. For this contribution, however, the incorrectly filtered parts of the water bottom were interactively removed. The resulting sigFWFS and volFWFS point clouds in Fig. 7 (c) and (d) show that the water bottom is plausibly represented up to a water depth of approx. $14.5\,\mathrm{m}$ with a high point density.

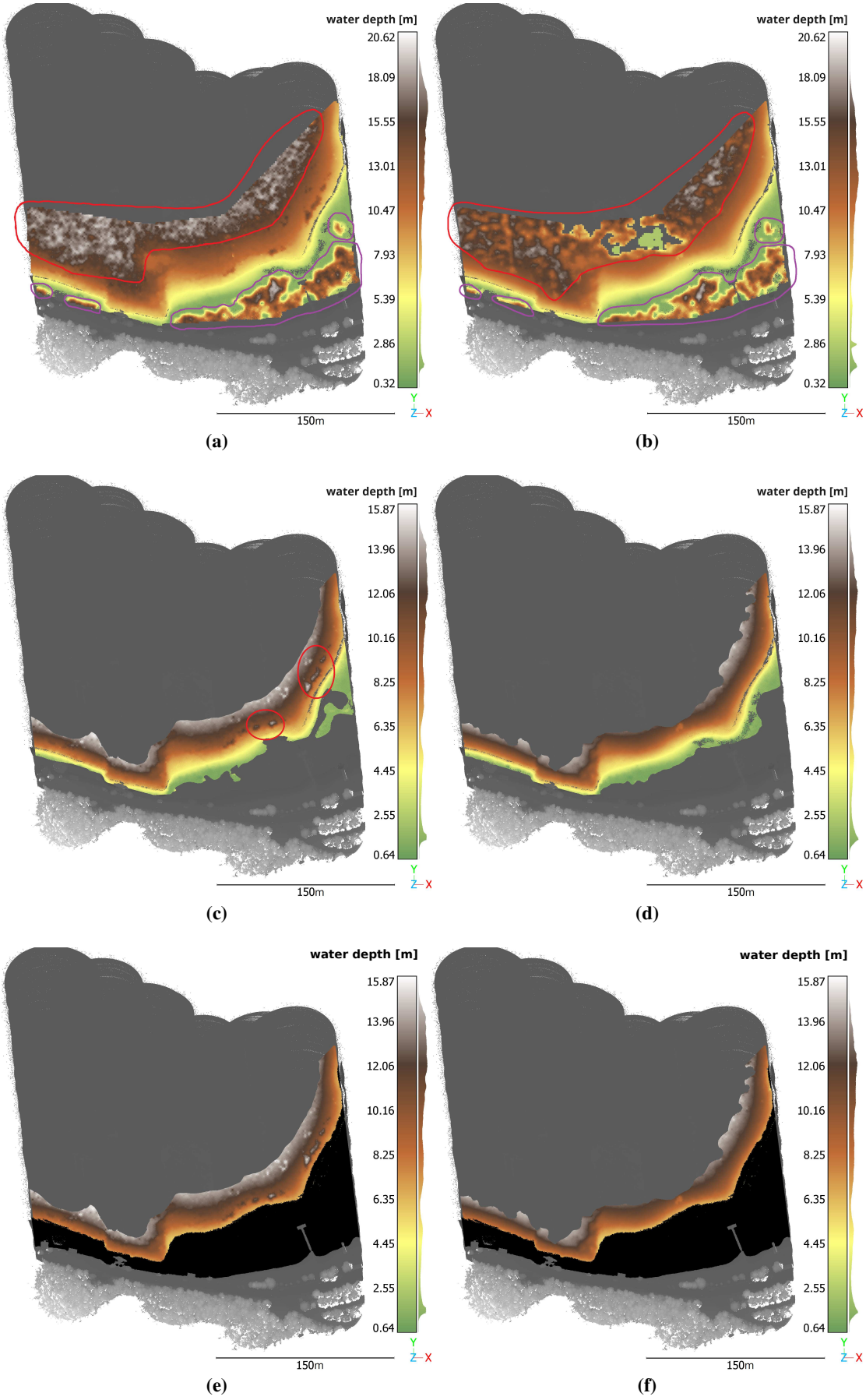

Figure 7. Top view of the point clouds resulting from sigFWFS (a) and volFWFS (b). The points are color coded according to their water depths. The problematic areas in the shallow water are marked in purple, the areas where the filtering has failed are marked in red. The results after interactive filtering are shown in (c) and (d). (e) and (f) show the coverage comparison between (c) and (d) and the OWP data (black points).

This contribution has been peer-reviewed.
https://doi.org/10.5194/isprs-archives-XLVIII-2-2024-341-2024

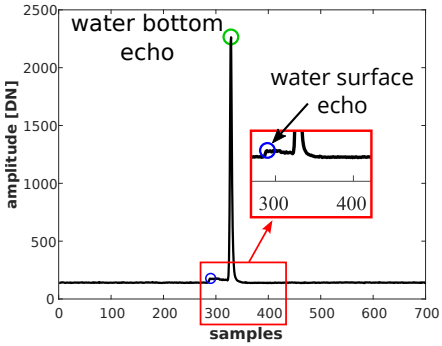

Figure 8. Full-waveform from the shallow water area of the study site (water depth $\leq 1.6\,\mathrm{m}$).

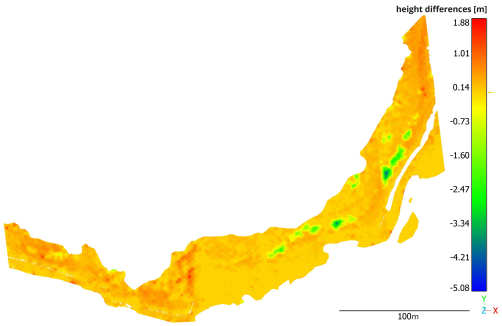

Figure 9. Comparison between sigFWFS and volFWFS point cloud color coded by their height differences (green = sigFWFS lower than volFWFS, red = sigFWFS higher than volFWFS).

Fig. 7 (c) clearly shows that even in the plausible areas there are isolated errors in the results of the sigFWFS processing. A comparison of the point clouds of sigFWFS and volFWFS shows no significant trend with an average height difference of $-0.004\,\mathrm{m}$. Fig. 9 shows the local differences between the point clouds.

Finally, the sigFWFS and volFWFS point clouds are validated by comparing them to the hydroacoustic measurements. Only points in the direct neighborhood of the hydroacoustic measurements (lateral distance $\leq 0.2\,\mathrm{m}$) were used to compare the height coordinates. The results of the point cloud comparisons are presented in Table 1. The statistical values used for the comparison correspond to those of (Mader et al., 2021, 2023a,b). Details on the calculation of the statistical values can be found in these articles.

If we consider the statistical values as a function of water depth, it is noticeable that the accuracy and reliability values for the results of the volFWFS are worse at smaller water depths than at larger water depths. Table 2 illustrates this by showing an example of the statistical values for the water depth range of $1\,\mathrm{m} - 7\,\mathrm{m}$ and $7\,\mathrm{m} - 15\,\mathrm{m}$. The accuracy and reliability of the sigFWFS results decreases with increasing water depth. Table 2 shows the statistical values for the same depth ranges as the results of the volFWFS.

In summary, it can be stated that the extracted water bottom points up to a water depth of approx. $14.5\,\mathrm{m}$ appear plausible. The comparison between sigFWFS and volFWFS also shows that the volFWFS overall worked better than the sigFWFS (Table 1). Table 2 shows that the volFWFS provided significantly better results than the sigFWFS, especially in the depth range of $7\,\mathrm{m} - 15\,\mathrm{m}$. This may be due to the fact that the sigFWFS does not take into account the laser beam direction when generating the pseudo-waveform. The result is a combination of full-waveforms that are close to each other at the water surface but not at the water bottom. This in turn causes the already weak bottom echo in the pseudo-waveform to be further ”smoothed” and thus less reliably detected when the water bottom is very sloped. It is evident that the penetration depth of both the sigFWFS and volFWFS processing is significantly larger than that of the standard processing (OWP), which was approximately $9.2\,\mathrm{m}$. Please note that the achieved water depth of the OWP data can vary depending on the parameter selection in the standard processing.

4. Determination of 3D turbidity parameter fields

This section first presents the full-waveform processing methods for determining 3D turbidity parameter fields (Section 4.1). The methods were applied to the pseudo-waveforms resulting from volFWFS. The results are presented and discussed in Section 4.2. For validation purposes, the water turbidity values determined from the UAV-based LiDAR bathymetry data are compared with the in-situ measurements.

4.1 Methods

Richter et al. (2022) present an approach for the determination of depth-resolved water turbidity parameters from pseudo-waveforms. In a first step the water column segment is extracted from the pseudo-waveform. For this purpose, the volume backscatter is defined as the signal component between the water surface and water bottom echo. For detection and extraction, the full-waveform analysis methods presented in Section 3.3 are used. Subsequently, a segment-wise exponential function approximation (sEFA) is carried out. For this purpose, several exponential segments are fitted into the water column part of the signal. The principle is shown schematically in Fig. 10. The sEFA provides an estimate of the exponential attenuation coefficients k_i, which represent a quantitative, integral, and non-metric measure of water turbidity in the water column.

The number of segments required is derived from the full-waveform itself. Based on the water surface echo, only the first part of the water column signal is initially taken into account in the exponential function approximation. In addition to the exponential attenuation coefficient, the quality of the approximation can be assessed using the RMS value from the fit of the measured values to the functional model. Subsequently, further samples are included step by step and the function approximation is repeated until the end of the water column signal is reached. Then, the RMS values of all function approximations are examined. The following cases can occur:

1. The water turbidity in the considered section is constant. The data are well described by the functional model and the RMS is small.
2. The considered part of the water column contains signal components from a different turbidity layer. The data are poorly described by the functional model. The more signal components of the different turbidity layer are included, the higher the RMS value.

An empirically determined threshold value is used to determine the point above which the RMS value increases (Fig. 10). A new exponential segment is added at this point. The process is repeated until all exponential segments have been found.

	sigFWFS	volFWFS
Accuracy		
$\Delta\bar{h}$	−0.13 m	−0.15 m
$\sigma_{\Delta\bar{h}}$	0.34 m	0.26 m
RMS	0.36 m	0.30 m
$\sigma_{MAD(median)}$	0.23 m	0.22 m
Inlier Rate (Litman et al., 2015)		
$\lvert\Delta h\rvert \leq$ IHO Depth TVU Special Order (25.0 cm – 27.4 cm; Value depends on depth)	62.39 %	62.65 %
$\lvert\Delta h\rvert \leq$ Depth TVU Order 1a (50.0 cm – 53.4 cm; Value depends on depth)	87.80 %	92.43 %

Table 1. Statistical comparison of the height coordinates of hydroacoustic measurements and sigFWFS or volFWFS. Negative values for $\Delta\bar{h}$ mean that sigFWFS and volFWFS are higher than the hydroacoustic measurements. The IHO Depth TVU Special Order/Order 1a was used for the inlier rate (International Hydrographic Organization, 2020).

	sigFWFS		volFWFS	
Water depth range	1 m – 7 m	7 m – 15 m	1 m – 7 m	7 m – 15 m
Accuracy				
$\Delta\bar{h}$	−0.119 m	−0.146 m	−0.180 m	−0.056 m
$\sigma_{\Delta\bar{h}}$	0.34 m	0.32 m	0.26 m	0.21 m
RMS	0.36 m	0.36 m	0.32 m	0.21 m
$\sigma_{MAD(median)}$	0.21 m	0.26 m	0.22 m	0.20 m
Inlier Rate (Litman et al., 2015)				
$\lvert\Delta h\rvert \leq$ IHO Depth TVU Special Order (25.0 cm – 27.4 cm; Value depends on depth)	65.58 %	52.79 %	58.76 %	77.25 %
$\lvert\Delta h\rvert \leq$ Depth TVU Order 1a (50.0 cm – 53.4 cm; Value depends on depth)	88.62 %	85.31 %	90.86 %	98.28 %

Table 2. Statistical comparison of the height coordinates of hydroacoustic measurements and sigFWFS or volFWFS for different water depth ranges. Negative values for $\Delta\bar{h}$ mean that sigFWFS and volFWFS are higher than the hydroacoustic measurements. The IHO Depth TVU Special Order/Order 1a was used for the inlier rate (International Hydrographic Organization, 2020).

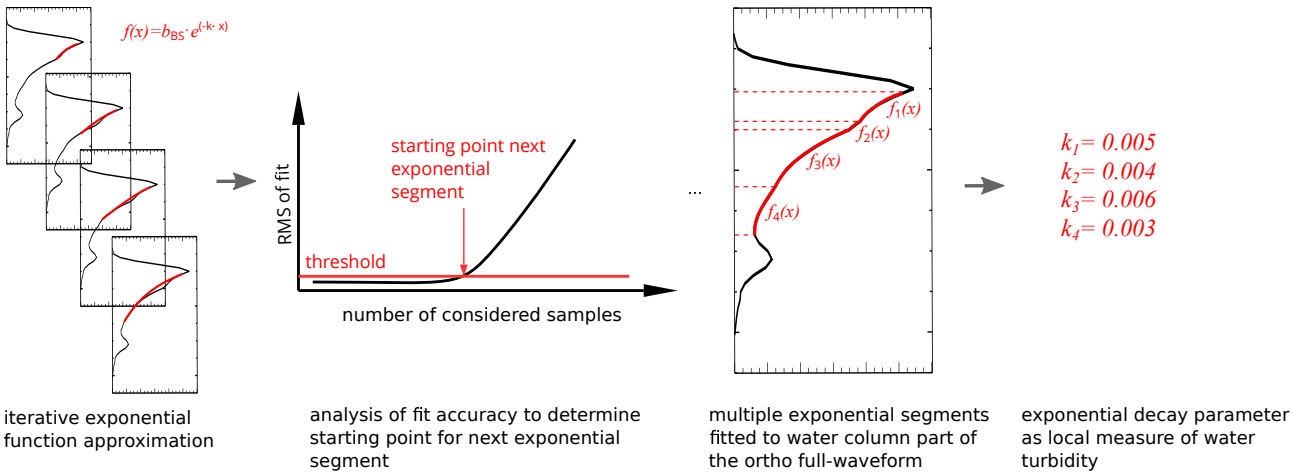

Figure 10. Schematic representation of the determination of depth-resolved water turbidity parameter fields by segment-wise exponential function approximation into the water column part of the ortho full-waveform.

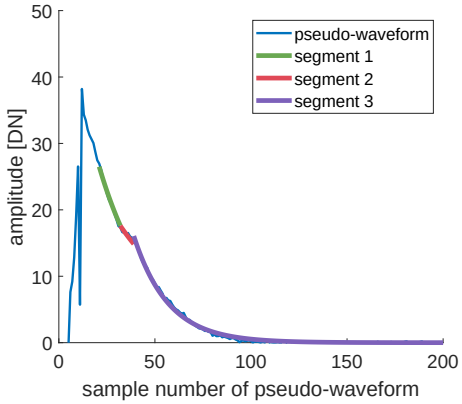

Figure 11. Derivation of depth-resolved water turbidity parameters from a volFWFS pseudo-waveform. The sample distance of the pseudo-waveform is 10 cm.

4.2 Results of high-resolution depth-resolved water turbidity parameter fields determination using sEFA

Figure 11 shows an example of the depth-resolved water turbidity parameters derived from a volFWFS pseudo-waveform. Three layers of different water turbidity were detected, extending from the water surface to a depth of 2.3 m (corresponding to 23 samples of the pseudo-waveform), from 2.3 m – 2.8 m (corresponding to 5 samples of the pseudo-waveform) and from 2.8 m to the maximum analyzable water depth of 14.5 m (corresponding to 117 samples of the pseudo-waveform). The detected turbidity stratification is confirmed by the reference measurements for water turbidity (Fig. 12). The evaluation of the measurements of the acquired local water characteristics (temperature, dissolved oxygen, pH value, conductivity, photosynthetically active radiation and chlorophyll concentration) has not yet been completed at the time of this publication.

Basically, ALB is used to investigate the properties of the water column in the green wavelength range. The water turbidity parameters derived from ALB data can therefore not be readily compared with the measurement results of other measurement methods. However, this also applies to conventional measurement methods, which examine different optical properties of the water column and are not compatible with each other. The area-wide and depth-resolved determination of water turbidity from ALB data or UAV-based LiDAR bathymetry data is a valuable addition to conventional point measurement methods and is ideally suited for describing spatio-temporal variations in water turbidity.

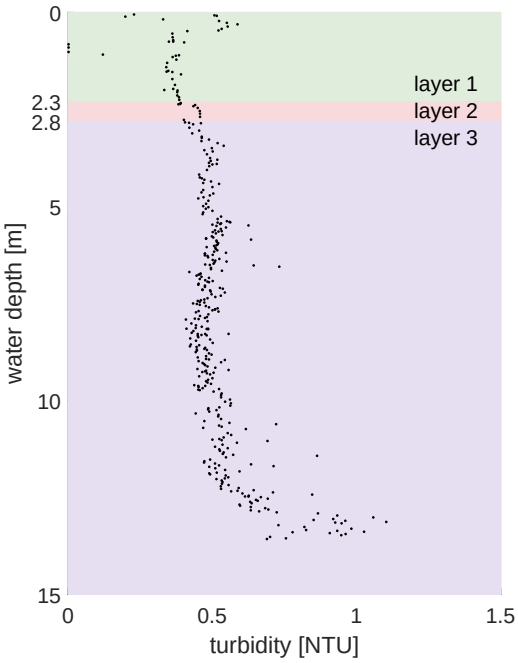

Figure 12. Results of the water turbidity measurement with the CTD probe.

5. Conclusion

The aim of this paper was to investigate the potential of full-waveform stacking evaluation methods on a water body with an analyzable water depth of more than 10 m and to validate the method of depth-resolved water turbidity parameter determination on the basis of water turbidity measurements. Both full-waveform stacking methods enable the detection of the water bottom up to a water depth of approx. 14.5 m. This corresponds to an increase in the analyzable water depth of about 58 % compared to the results of the standard processing (OWP data), whereby the specific value depends on the parameters used for the OWP. In the UAV-based LiDAR bathymetry data, three layers of different water turbidity were detected, which was confirmed by the in-situ water turbidity measurements. The results presented here are part of the first investigations carried out on this data set. Future work will focus on the following aspects:

1. enhancement of full-waveform stacking filter methodology for water bottom topographies with larger and more dynamic gradients;
2. investigation of the influence of different laser beam divergences on the results of OWP, full-waveform stacking processing methods, and determination of depth-resolved water turbidity parameter fields;
3. further investigation of the performance of sigFWFS and volFWFS by comparison with refraction-corrected OWP data and hydroacoustic measurements;
4. comprehensive validation of depth-resolved water turbidity parameters including all in-situ measurements.

6. Acknowledgement

The work on laser bathymetry is funded by the German Research Foundation (DFG). The aerial survey and data processing with standard processing procedures were carried out by the company skyability GmbH. We would like to thank the entire skyability GmbH team for their excellent cooperation, their prompt response to our queries and their interest in our research. We would also like to thank Dr. Thomas Petzoldt from the Chair of Limnology (TU Dresden) for his expertise and for carrying out the measurements of the water characteristics. We would also like to thank the Chair of Limnology (TU Dresden) for providing the measurement sensors.

References

Anderson, J. T., Holliday, D. V., Kloser, R., Reid, D., Simard, Y., Brown, C. J., 2007. Acoustic seabed classification of marine physical and biological landscapes. Technical report, International Council for the Exploration of the Sea.

International Hydrographic Organization, 2020. IHO Standards for Hydrographic Surveys, 6th Edition, IHO Special Publication S-44. International Hydrographic Organization.

Litman, R., Korman, S., Bronstein, A., Avidan, S., 2015. Inverting ransac: Global model detection via inlier rate estimation. *Proceedings of the IEEE conference on computer vision and pattern recognition*, 5243–5251.

Mader, D., Richter, K., Westfeld, P., Maas, H.-G., 2021. Potential of a Non-linear Full-Waveform Stacking Technique in Airborne LiDAR Bathymetry. *PFG–Journal of Photogrammetry, Remote Sensing and Geoinformation Science*, 89, 139–158.

Mader, D., Richter, K., Westfeld, P., Maas, H.-G., 2023a. Volumetric nonlinear ortho full-waveform stacking in airborne LiDAR bathymetry for reliable water bottom point detection in shallow waters. *ISPRS Journal of Photogrammetry and Remote Sensing*, 204, 145–162.

Mader, D., Richter, K., Westfeld, P., Nistad, J.-G., Maas, H.-G., 2023b. Analysis of the potential of full-waveform stacking techniques applied to coastal airborne LiDAR bathymetry data of the German Wadden Sea National Park. *International Hydrographic Review*, 29(2), 46 - 64.

Mallet, C., Bretar, F., 2009. Full-waveform topographic lidar: State-of-the-art. *ISPRS Journal of Photogrammetry and Remote Sensing*, 64(1), 1–16.

Mandlburger, G., Monetti, D., Greifeneder, C., 2022. Fließgewässervermessung mittels UAV-basierter Laserbathymetrie im Produktiveinsatz. *Österreichische Zeitschrift für Vermessung und Geoinformation (VGI)*, 2022(2), 59–77.

Mandlburger, G., Pfennigbauer, M., Schwarz, R., 2020. Genauigkeits-und performanceuntersuchung eines neuen bathymetrischen uav-laserscanners. *40. Wissenschaftlich-Technische Jahrestagung der DGPF in Stuttgart*, Publikationen der DGPF, 321–334.

Pfennigbauer, M., Rieger, P., Studnicka, N., Ullrich, A., 2009. Detection of concealed objects with a mobile laser scanning system. *Laser Radar Technology and Applications XIV*, 7323, SPIE, 51–59.

Pfennigbauer, M., Ullrich, A., 2010. Improving quality of laser scanning data acquisition through calibrated amplitude and pulse deviation measurement. *Laser Radar Technology and Applications XV*, 7684, SPIE, 463–472.

Reitberger, J., Schnörr, C., Krzystek, P., Stilla, U., 2009. 3D segmentation of single trees exploiting full waveform LiDAR data. *ISPRS Journal of Photogrammetry and Remote Sensing*, 64(6), 561–574.

Richter, K., Maas, H.-G., Westfeld, P., Weiß, R., 2017. An approach to determining turbidity and correcting for signal attenuation in airborne lidar bathymetry. *PFG–Journal of Photogrammetry, Remote Sensing and Geoinformation Science*, 85(1), 31–40.

Richter, K., Mader, D., Westfeld, P., Maas, H.-G., 2021. Water turbidity estimation from lidar bathymetry data by full-waveform analysis - comparison of two approaches. *The International Archives of the Photogrammetry, Remote Sensing and Spatial Information Sciences*, Volume XLIII-B2-2021.

Richter, K., Mader, D., Westfeld, P., Maas, H.-G., 2022. Determination of 3d Water Turbidity Parameter Fields from LIDAR Bathymetry Data by Volumetric Data Analysis. *The International Archives of the Photogrammetry, Remote Sensing and Spatial Information Sciences*, 43, 945–951.

Sardemann, H., Eltner, A., Maas, H.-G., 2018. Acquisition of geometrical data of small rivers with an unmanned water vehicle. *The International Archives of the Photogrammetry, Remote Sensing and Spatial Information Sciences*, 42, 1023–1027.

Saylam, K., Hupp, J. R., Andrews, J. R., Averett, A. R., Knudby, A. J., 2018. Quantifying airborne lidar bathymetry quality-control measures: a case study in Frio river, Texas. *Sensors*, 18(12), 4153.

Schwarz, R., Mandlburger, G., Pfennigbauer, M., Pfeifer, N., 2019. Design and evaluation of a full-wave surface and bottom-detection algorithm for LiDAR bathymetry of very shallow waters. *ISPRS journal of photogrammetry and remote sensing*, 150, 1–10.

Schwarz, R., Pfeifer, N., Pfennigbauer, M., Ullrich, A., 2017. Exponential decomposition with implicit deconvolution of lidar backscatter from the water column. *PFG–Journal of Photogrammetry, Remote Sensing and Geoinformation Science*, 85(3), 159–167.

Secchi, P. A., 1864. Relazione delle esperienze fatte a bordo della pontificia pirocorvetta Imacolata Concezione per determinare la trasparenza del mare. *Il Nuovo Cimento*, 20(1), 205–238.

Wagner, W., Ullrich, A., Ducic, V., Melzer, T., Studnicka, N., 2006. Gaussian decomposition and calibration of a novel small-footprint full-waveform digitising airborne laser scanner. *ISPRS Journal of Photogrammetry and Remote Sensing*, 60(2), 100–112.

Wagner, W., Ullrich, A., Melzer, T., Briese, C., Kraus, K., 2004. From single-pulse to full-waveform airborne laser scanners: potential and practical challenges. *International Archives of Photogrammetry, Remote Sensing and Spatial Information Sciences*, 35(3), 201–206.

Wang, C., Li, Q., Liu, Y., Wu, G., Liu, P., Ding, X., 2015. A comparison of waveform processing algorithms for single-wavelength LiDAR bathymetry. *ISPRS Journal of Photogrammetry and Remote Sensing*, 101, 22–35.